

around at the bottom of the CB with mid-IR or terahertz driving fields is impossible (23, 24). Our results, however, prove that it is possible to observe the DFKE driven by femtosecond IR pulses at energies high above the band gap. We have also shown that the fine structure in the transient response of diamond deviates from the simplified parabolic model and thus encodes information about the particular band dispersion of the target.

REFERENCES AND NOTES

1. D. H. Auston, K. P. Cheung, J. A. Valdmantis, P. R. Smith, *Picosecond Electronics and Optoelectronics* (Springer-Verlag, 1985).
2. D. H. Auston, *Top. Appl. Phys.* **60**, 183 (1988).
3. D. Grischkowsky, S. Keiding, M. van Exter, C. Fattinger, *J. Opt. Soc. Am. B* **7**, 2006 (1990).
4. G. Steinmeyer, D. H. Sutter, L. Gallmann, N. Matuschek, U. Keller, *Science* **286**, 1507–1512 (1999).
5. P. M. Paul et al., *Science* **292**, 1689–1692 (2001).
6. M. Hentschel et al., *Nature* **414**, 509–513 (2001).
7. H. Telle et al., *Appl. Phys. B* **69**, 327–332 (1999).
8. E. Goulielmakis et al., *Nature* **466**, 739–743 (2010).
9. H. Wang et al., *Phys. Rev. Lett.* **105**, 143002 (2010).
10. M. Holler, F. Schapper, L. Gallmann, U. Keller, *Phys. Rev. Lett.* **106**, 123601 (2011).
11. M. Schultze et al., *Nature* **493**, 75–78 (2013).
12. M. Schultze et al., *Science* **346**, 1348–1352 (2014).
13. H. Mashiko, K. Oguri, T. Yamaguchi, A. Suda, H. Gotoh, *Nat. Phys.* **10**, 1038/nphys3711 (2016).
14. F. Krausz, M. I. Stockman, *Nat. Photonics* **8**, 205–213 (2014).
15. H. J. Caulfield, S. Dolev, *Nat. Photonics* **4**, 261–263 (2010).
16. A. H. Chin, J. M. Bakker, J. Kono, *Phys. Rev. Lett.* **85**, 3293–3296 (2000).
17. Y. Mizumoto, Y. Kayanuma, A. Srivastava, J. Kono, A. H. Chin, *Phys. Rev. B* **74**, 045216 (2006).
18. A. P. Jauho, K. Johnsen, *Phys. Rev. Lett.* **76**, 4576–4579 (1996).
19. G. H. Wannier, *Elements of Solid State Theory* (Cambridge Univ. Press, 1960).
20. G. Vampa et al., *Nature* **522**, 462–464 (2015).
21. T. T. Luu et al., *Nature* **521**, 498–502 (2015).
22. P. Y. Yu, M. Cardona, *Fundamentals of Semiconductors* (Springer, ed. 4, 2010).
23. F. Novelli, D. Fausti, F. Giusti, F. Parmigiani, M. Hoffmann, *Sci. Rep.* **3**, 1227 (2013).
24. A. Srivastava, R. Srivastava, J. Wang, J. Kono, *Phys. Rev. Lett.* **93**, 157401 (2004).
25. K. B. Nordstrom et al., *Phys. Rev. Lett.* **81**, 457–460 (1998).
26. R. Locher et al., *Rev. Sci. Instrum.* **85**, 013113 (2014).
27. See supplementary materials on Science Online.
28. L. V. Keldysh, *Sov. Phys. J. Exp. Theor. Phys.* **20**, 1307 (1965).
29. S. A. Sato, K. Yabana, Y. Shinohara, T. Otobe, G. F. Bertsch, *Phys. Rev. B* **89**, 064304 (2014).
30. K. Yabana, T. Sugiyama, Y. Shinohara, T. Otobe, G. F. Bertsch, *Phys. Rev. B* **85**, 045134 (2012).
31. W. V. Houston, *Phys. Rev.* **57**, 184–186 (1940).
32. T. Otobe, Y. Shinohara, S. A. Sato, K. Yabana, *Phys. Rev. B* **93**, 045124 (2016).

ACKNOWLEDGMENTS

Supported by the National Center of Competence in Research Molecular Ultrafast Science and Technology (NCCR MUST) funded by the Swiss National Science Foundation, and by JSPS KAKENHI grants 15H03674 and 26-1511. This research used computational resources of the K computer provided by RIKEN AICS through the HPCI System Research project (Project ID hp150101), and was supported in part by MEXT as a priority issue theme 7 to be tackled by using Post K Computer.

SUPPLEMENTARY MATERIALS

www.sciencemag.org/content/353/6302/916/suppl/DC1
Materials and Methods
Figs. S1 to S13
References (33–45)

12 May 2016; accepted 27 July 2016
10.1126/science.aag1268

GEOPHYSICS

Teleseismic *S* wave microseisms

Kiwamu Nishida^{1*} and Ryota Takagi²

Although observations of microseisms excited by ocean swells were firmly established in the 1940s, the source locations remain difficult to track. Delineation of the source locations and energy partition of the seismic wave components are key to understanding the excitation mechanisms. Using a seismic array in Japan, we observed both *P* and *S* wave microseisms excited by a severe distant storm in the Atlantic Ocean. Although nonlinear forcing of an ocean swell with a one-dimensional Earth model can explain *P* waves and vertically polarized *S* waves (*SV* waves), it cannot explain horizontally polarized *S* waves (*SH* waves). The precise source locations may provide a new catalog for exploring Earth's interior.

Microseisms are ambient seismic wavefields (*I*) that occur in the 0.05- to 0.5-Hz frequency range. Although they had been recognized as ambient noise for seismic observation, a new technique known as seismic interferometry turned them into signals for exploring Earth's interior (2). They can be categorized into two groups according to the typical frequencies. The first group is classified as primary microseisms ranging from 0.05 to 0.1 Hz, which corresponds to the typical frequency of ocean swells. The second is classified as secondary microseisms ranging from 0.1 to 0.5 Hz, which doubles the frequency of an ocean swell, indicating that the secondary microseisms are generated through nonlinear wave-wave interactions (3, 4). They excite surface waves dominantly.

P wave microseisms from distant storms have been studied (5, 6) by means of array analysis of dense seismic data. Source locations of the *P* wave provided a better spatial localization of the excitation source than that of surface waves. The estimated source distribution was consistent with a theoretical estimation that uses wave action models. Most studies, however, have focused only on *P* waves recorded as vertical components because of the larger amplitudes. Although *S* wave amplitudes are estimated to be one order of magnitude smaller than *P* wave amplitudes (7, 8), the precise locations of *P* and *S* waves can help in understanding the excitation mechanism.

The energy partition between Love and Rayleigh waves is another key parameter for understanding the force system of excitation sources. The force system can be characterized by the surface pressure source and/or shear traction on the seafloor (9). The observed dominance of Love waves in primary microseisms suggests that they are generated by pressure loadings of an ocean swell acting on a sloping coast (10). However, the scattering of surface waves during propagation distorts the energy ratio at the source area. Because the teleseismic body waves are less scattered, the energy partition between *P* and *S* waves is more appropriate for understanding the source mechanism. However, the smaller body-wave amplitudes at a distance

tend to be masked by the surface waves owing to local ocean swell activities (8, 11, 12).

For the detection of both *P* and *S* wave microseisms, we conducted an array analysis using 202 Hi-net stations operated by the National Research Institute for Earth Science and Disaster Prevention (NIED) in Chugoku district, where the crustal heterogeneity is weak in Japan (Fig. 1A). NIED deployed three-component velocity meters with a natural frequency of 1 Hz at the bottom of a borehole of each station. We deconvolved the instrumental response using the inverse filtering technique (13) after the reduction of common logger noise (14) so as to use low-frequency components below 1 Hz. We analyzed data of a rapidly deepening cyclonic low-pressure area known as a “weather bomb” (15), with a central pressure of ~940 hPa that developed in the Atlantic between Iceland and Greenland on 9–11 December 2014 (16). The system was a typical explosive cyclogenesis, with a reduction of 24 hPa in 24 hours on 9 December. We divided the records into 1024-s segments. After the exclusion of noisy data, we calculated two-dimensional (2D) frequency-slowness spectra (9) in the 0.1- to 0.2-Hz frequency window (Fig. 1B), assuming that signals at a station can be represented by a superposition of plane waves. The spectrum at a certain slowness vector represents the sum of all the records, with the predicted time delays. The spectra have local maxima in the slowness domain, where signals recorded at all the stations are in phase.

The spectra of the vertical and radial components displayed a clear teleseismic *P* wave. The slowness of ~0.05 s/km and the back azimuth of ~5° were consistent with that of a *P* wave traveled from the Atlantic Ocean. The dominant *P* wave can be explained by the nonlinear forcing by ocean swell (7) according to Longuet-Higgins's theory (3), which can be equivalently represented by a vertical single force on the sea surface.

The spectrum of the radial component showed not only a *P* wave but also a rarely seen *SV* wave (8), with mean square (MS) amplitude of ~8% of the *P* wave amplitude. The observed slowness of the *SV* wave suggests that the source could be located in the same area of the *P* wave microseisms in the Atlantic Ocean. The simplest mechanism of the observed *S* wave excitation is the *P*-to-*SV* conversion on the sea bottom during multiple reflections within the ocean (7). Although the theoretical MS amplitude (7) of an *SV* wave is two orders smaller than

¹Earthquake Research Institute, University of Tokyo, 1-1-1 Yayoi 1, Bunkyo-ku, Tokyo 113-0032, Japan. ²Research Center for Prediction of Earthquakes and Volcanic Eruptions, Graduate School of Science, Tohoku University, 6-6 Aza-Aoba, Aramaki, Aoba-ku, Sendai 980-8578, Japan.

*Corresponding author. E-mail: knishida@eri.u-tokyo.ac.jp

Fig. 1. Rough source location estimated by back-projection of the observed body-wave microseisms. (A) Station distribution and location of the weather bomb. Red points in Japan indicate the station locations used in the slowness-frequency analysis. Black and red dots indicate all the Hi-net station locations. The red dashed line represents 0.5 of the array response function for a point source at $(-32.5, 63)$, indicated with the red star. The trapezoid region indicates the area shown in Fig. 2A. The location of the earthquake is indicated by the yellow star. **(B)** Frequency-slowness spectra of radial, transverse, and vertical components at 0.15 Hz. This figure shows the *P* wave traveling from the north direction with back azimuth of $\sim -7^\circ$. The slowness is ~ 0.048 s/km, which determined the distance between the source and the receivers as shown in (A).

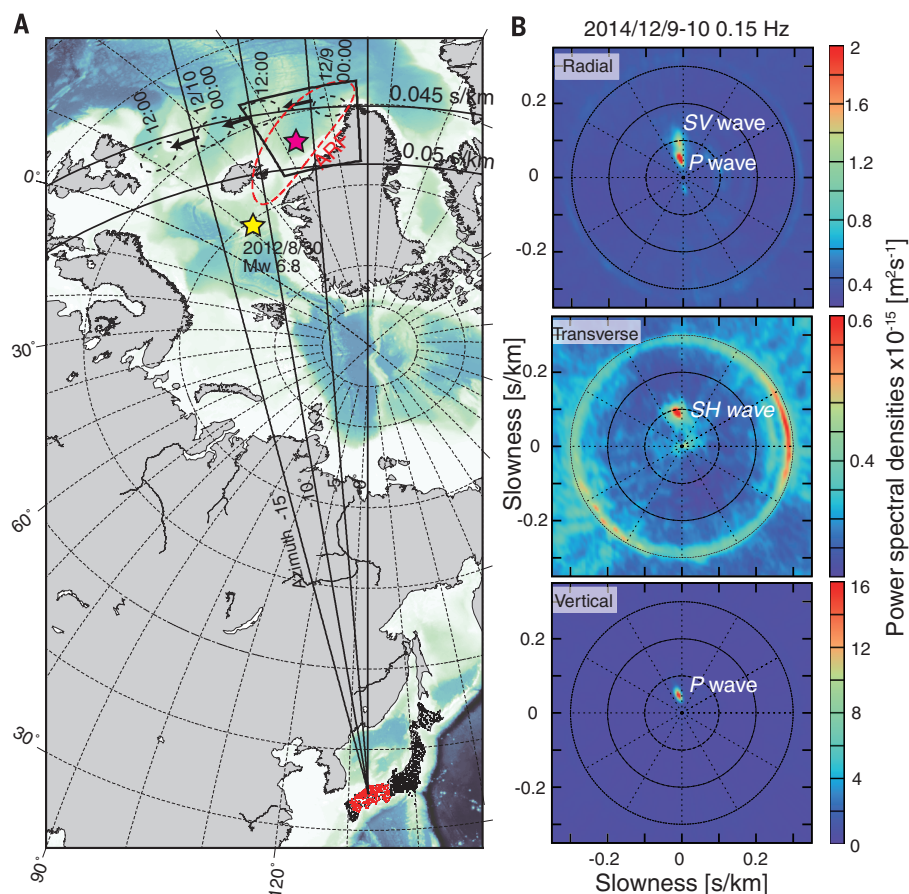


Fig. 2. Migration of precise centroid locations of *P*, *SV*, and *SH* waves. (A) Locations of the centroids with errors $<1.5^\circ$ in latitude and longitude. The error was estimated with the bootstrap method (23). Orange dots indicate the centroids of the *P* wave microseisms. Purple triangles indicate the *SV* waves. Blue stars indicate the *SH* wave. The background image shows the site effect of the ocean layer, whereas the contours show the resonant frequency of the sediment. The resonant frequency was estimated by means of a four-way travel time of multiple reflection of sediment-derived *S* waves in the vertical direction. (i) through (v) represent time labels every 12 hours, as shown in (B). **(B)** Latitude of centroids of *P*, *SH*, and *SV* waves with respect to time. **(C)** Longitude of the centroids with respect to time. This figure shows that source locations of *SH* wave at 0 hours on 10 December were west of the others. **(D)** Temporal variations of RMS amplitudes of the single force. The black line shows a synthetic vertical single force (20).

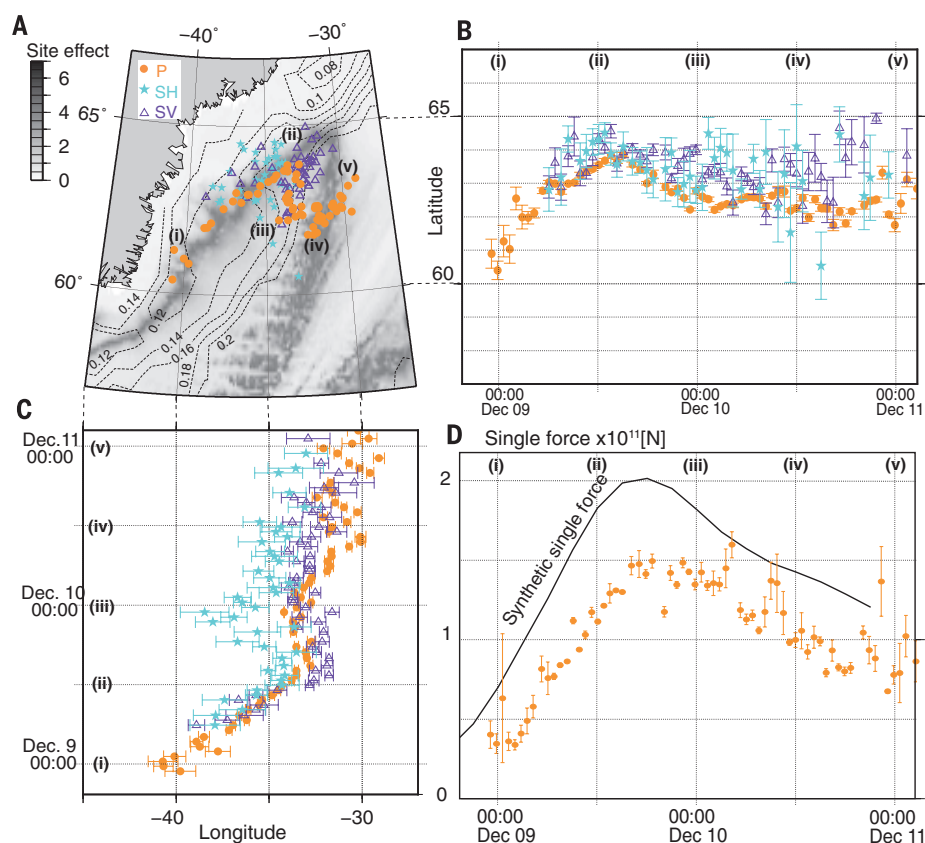
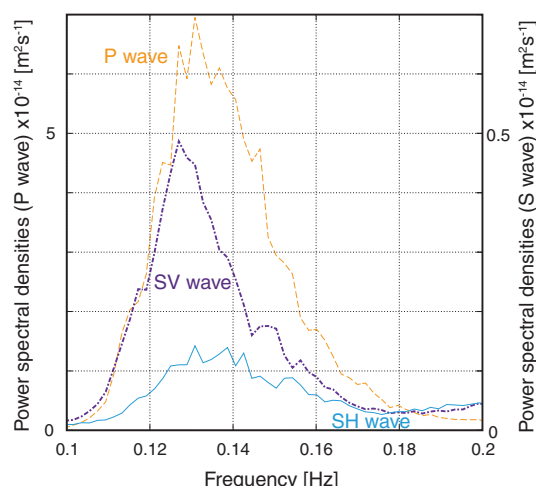


Fig. 3. Stacked power spectra of *P*, *SV*, and *SH* waves. Orange dashed line, *P* wave; purple dash-dotted line, *SV* wave; blue line, *SH* wave. They are power spectra of the seismograms of vertical (*P* wave), radial (*SV* wave), and transverse components (*SH* wave), with shift in time according to the corresponding travel times for the located centroids from 9 to 11 December 2014. The power spectral densities of the *SV* waves were 8% of the *P* wave. The *SH* waves consisted of one third of those for the *SV* waves. The peak frequencies of *P*, *SV*, and *SH* waves were ~0.13 Hz.



that of a *P* wave, the amplitude depends strongly on the incident angle. Within the possible range on the basis of different 1D seismic velocity models, our observation is consistent with the prediction.

Surprisingly, the spectrum of the transverse component also showed an *SH* wave microseism. A pressure source in the ocean cannot excite the *SH* waves in a spherically stratified Earth. Therefore, the shear traction acting on the sea-bottom horizon is required. This observation suggests that the steep topography beneath the source and thick sediments may affect the excitation. The smaller recorded amplitude of ~3% of the *P* wave MS amplitude suggests that this effect is secondary.

We inferred the centroid locations of *P* wave microseisms with a method that is similar to the GRiD MT (grid-based real-time determination of moment tensors) technique (17). We modeled the localized excitation source by approximating the source using a vertical single force at a surface point. We characterized the source by the centroid location and the root mean square (RMS) amplitude of the single force. We justify the point source approximation as the localized source area was on the order of 10^5 km², which we estimated by using the wave model WAVEWATCH III (fig. S1) (18, 19) and which is smaller than the array response function (Fig. 1A). At an assumed grid point, we estimated RMS of the vertical single force by modeling the seismic wave fields using a ray-theory *P* wave Green's function (20) for a 1D Earth model (21). The variance reductions between the modeled wave field and the observations were calculated at assumed grid points every 0.1° by 0.1° in longitude and latitude. The maximum was selected as the centroid location for the vertical single force. We subtracted the station correction terms using a multichannel cross-correlation method (22) with an earthquake that occurred close to Iceland on 30 August 2012 (Fig. 1A) because 3D seismic structure biases the locations of the centroids. Without the station corrections, the centroid of the earthquake located by this method deviated ~300 km away from the original location. Orange dots in Fig. 2A represent the locations of the centroids inferred from the vertical components at 775 stations. RMSs of the centroid single force were on the order of 10^{11} N

(Fig. 2D). They were consistent with the theoretical estimation of the wave model (fig. S2) and a previous study (12). The inferred centroid locations were consistent with a theoretical model (fig. S1). The centroids migrated along an area that contains a strong site effect (7) of the ocean layer. This can be described as the constructive interference of multiply reflected *P* waves in the ocean that are converted to *P* and *SV* waves at the sea bottom (7). The site effect becomes larger where the resonance frequency of the oceanic layer matches the *P* wave frequency. From time period (i) to (ii) shown in Fig. 2A, the centroids migrated along the strong site effect area. From (ii) to (iv), they were not in the area. From (iv) to (v), they migrated along the area again. We can explain this observation from (ii) to (iv) by the larger source area (fig. S1), including both the part from (i) to (ii) and that from (iv) to (v) in Fig. 2A with the strong site effects. This method determined the centroids of the distributed sources with weighting by the site effects.

We located centroids of the *SH* and *SV* waves by back-projecting the seismograms in the horizontal components with the station corrections (24). We did not estimate the equivalent single force because modeling is not practical, owing to the near source amplification from multiple reflections in the ocean and sedimentary layers. The centroid locations of the *SH* and *SV* waves are shown with a resonant frequency of the sediment (Fig. 2A) (20) that corresponds to the fundamental mode in a closed pipe system, based on CRUST1.0 (25). Our centroid locations of the *SV* waves were close to the *P* wave centroids. However, our centroid locations of the *SH* waves were to the west [in particular at around (iii)], as shown in Fig. 2C], where the sediments have lower resonant frequencies closer to the *SH* wave frequency, as we observed (Fig. 2B). Our observation suggests *SH* waves trapped in the sedimentary layer. Moreover, the peak frequency of the *SH* wave at 0.13 Hz was similar to those of the *P* and *SV* waves (Fig. 3). We suggested the transfer of a large part of the *SV* wave energy into the sediments from the *P* wave to explain the frequency overlap, in which the sedimentary resonant frequency matched the dominant frequency of the *P*

wave microseisms. During multiple reflections of the *SV* wave in the sediment, the polarization information was lost, and part of the *SV* wave energy was converted to the *SH* wave over time (20).

Body-wave microseisms provide information about Earth's deep interior beneath the stations via seismic interferometry (26), which extracts seismic-wave propagation between station pairs. We have characterized the excitation source by a centroid vertical single force (3, 4, 7). Hence, the seismic structure beneath a storm can be explored by using body-wave microseisms. Because the estimated vertical single force is consistent with a former study (12), we can expect similar potential events with amplitude on the order of 10^{11} N. A collection of precise locations of the centroid single force may provide a catalog for exploring Earth's interior. Such a catalog may open a different perspective from which to explore Earth's deep interior beneath a storm in the absence of seismic stations and earthquakes.

REFERENCES AND NOTES

- B. Gutenberg, *J. Atmos. Sci.* **4**, 21 (1947).
- R. Snieder, E. Larose, *Annu. Rev. Earth Planet. Sci.* **41**, 183–206 (2013).
- M. S. Longuet-Higgins, *Phil. Trans. Roy. Soc. A* **243**, 1–35 (1950).
- S. Kedar et al., *Proc. R. Soc. London Ser. A* **464**, 777–793 (2008).
- P. Gerstoft, M. C. Fehler, K. G. Sabra, *Geophys. Res. Lett.* **33**, L17308 (2006).
- M. Landès, F. Hubans, N. M. Shapiro, A. Paul, M. Campillo, *J. Geophys. Res.* **115** (B5), B05302 (2010).
- L. Gualtieri et al., *Geophys. J. Int.* **197**, 1096–1106 (2014).
- Q. Liu et al., *Earth Planet. Sci. Lett.* **449**, 39–47 (2016).
- K. Nishida, H. Kawakatsu, Y. Fukao, K. Obara, *Geophys. Res. Lett.* **35**, L16307 (2008).
- F. Ardhuin, L. Gualtieri, E. Stutzmann, *Geophys. Res. Lett.* **42**, 765–772 (2015).
- M. N. Toksöz, R. T. Lacoss, *Science* **159**, 872–873 (1968).
- L. Vinick, *Pure Appl. Geophys.* **103**, 282–289 (1973).
- T. Maeda, K. Obara, T. Furumura, T. Saito, *J. Geophys. Res.* **116** (B10), B10303 (2011).
- R. Takagi et al., *Seismol. Res. Lett.* **86**, 901–907 (2015).
- T. Matsuzawa, K. Obara, T. Maeda, Y. Asano, T. Saito, *Bull. Seismol. Soc. Am.* **102**, 1864–1871 (2012).
- Weather* **70**, 54 (2015).
- H. Kawakatsu, *Bull. Earth. Res. Inst.* **73**, 267–274 (1998).
- H. L. Tolman, *Ocean Model.* **25**, 35–47 (2008).
- F. Ardhuin, E. Stutzmann, M. Schimmel, A. Mangueney, *J. Geophys. Res.* **116** (C9), 1–21 (2011).
- Materials and methods are available as supplementary materials on Science Online.
- B. L. Kennett, E. R. Engdahl, R. Buland, *Geophys. J. Int.* **122**, 108–124 (1995).
- J. VanDecar, R. S. Crosson, B. Y. J. C. Vandecar, R. S. Crosson, *Bull. Seismol. Soc. Am.* **80**, 150–169 (1990).
- B. Efron, *Ann. Stat.* **7**, 1–26 (1979).
- M. Ishii, P. M. Shearer, H. Houston, J. E. Vidale, *Nature* **435**, 933–936 (2005).
- G. Laske, G. Masters, Z. Ma, M. Pasyanos, Update on CRUST1.0—A 1-degree Global Model of Earth's Crust, *EGU General Assembly Conference Abstracts* (2013), vol. 15 of *EGU General Assembly Conference Abstracts*, pp. EGU2013-EGU2658.
- P. Poli, M. Campillo, H. Pedersen, LAPNET Working Group, *Science* **338**, 1063–1065 (2012).

ACKNOWLEDGMENTS

We thank S. Kedar, an anonymous reviewer, and E. Stutzmann for constructive comments. Hi-net seismic records were provided by NIED at www.hinet.bosai.go.jp. This work was supported by Japan Society for the Promotion of Science KAKENHI grants 26400448 and 15J11322.

SUPPLEMENTARY MATERIALS

www.sciencemag.org/content/353/6302/919/suppl/DC1
Materials and Methods
Figs. S1 to S3
References (27–31)

25 March 2016; accepted 25 July 2016
10.1126/science.aaf7573

Teleseismic S wave microseisms

Kiwamu Nishida and Ryota Takagi

Science **353** (6302), 919-921.
DOI: 10.1126/science.aaf7573

A seismic "weather bomb" detector

Seismic tomography is like an x-ray of Earth's interior, except that it uses earthquakes for the illumination. Earthquakes are imperfect illuminators because they are clustered on plate boundaries, leaving much of the interior in the shadows. Using a seismic array in Japan, Nishida and Takagi detected seismic waves that they attribute to a severe and distant North Atlantic storm called a "weather bomb" (see the Perspective by Gerstoft and Bromirski). The seismic energy traveling from weather bombs through the Earth appears to be capable of illuminating the many dark patches of Earth's interior.

Science, this issue p. 919; see also p. 869

ARTICLE TOOLS

<http://science.sciencemag.org/content/353/6302/919>

SUPPLEMENTARY MATERIALS

<http://science.sciencemag.org/content/suppl/2016/08/24/353.6302.919.DC1>

RELATED CONTENT

<http://science.sciencemag.org/content/sci/353/6302/869.full>

REFERENCES

This article cites 27 articles, 7 of which you can access for free
<http://science.sciencemag.org/content/353/6302/919#BIBL>

PERMISSIONS

<http://www.sciencemag.org/help/reprints-and-permissions>

Use of this article is subject to the [Terms of Service](#)